





A Simplified Theory of External Occulters for Solar Coronagraphs

CRAIG. E. DEFOREST ¹, NICHOLAS F. ERICKSON ¹, MATTHEW N. BEASLEY ¹, STEVEN N. OSTERMAN ¹,
TRAVIS J. SMITH ¹ AND MARY H. HANSON ¹

¹*Southwest Research Institute
1301 Walnut St., Suite 400
Boulder, CO, 80302, USA*

Submitted to Astrophysical Journal; Accepted 23-Dec-2024

ABSTRACT

We present a first-principles analytic treatment of modern multi-vane occulters in circular (coronagraph) and linear (heliospheric imager) geometry, develop a simplified theory that is useful for designing and predicting their performance, explain certain visual artifacts, and explore the performance limits of multi-vane occulters. Multi-vane occulters are challenging to design in part because they violate the conditions for both the Fraunhofer and Fresnel approximations to diffraction theory, and new designs have therefore generally required explicit simulation, empirical measurement, “guesstimation”, or all three. Starting from the Kirchoff diffraction integral, we develop a “sequential plane wave” approximate analytic theory that is suitable for predicting performance of multi-vane occulters, and use it to derive closed-form expressions for the performance of new designs. We review the fundamental 2-D system of an occulter edge, discuss how it applies to real 3-D systems by extrusion or revolution, present the reason for observed bright quasi-achromatic fringing around coronagraph occulters, develop the sequential plane wave approximation in 2-D and explore its limits, describe the relevance of the 2-D theory to practical 3-D instruments, and discuss implications for multi-vane occulter design in current and future instruments.

Keywords: Solar instruments (1499) — Coronagraphic imaging (313) — Astronomical optics (88) — Optical observation (1169)

1. INTRODUCTION

The solar corona, viewed in visible light, has roughly one millionth the total intensity of the solar photosphere. The contrast is so large that the corona is not normally visible without a total solar eclipse. Imaging the corona under normal conditions requires specialized equipment to reject light from the much brighter solar photosphere. The technology of specific coronagraph instruments has been described by many authors as the technology has developed over the past century (e.g., Lyot 1930; Evans 1948; Newkirk & Bohlin 1963; Koomen et al. 1975; Brueckner et al. 1995; Howard et al. 2008; Yang et al. 2018; DeForest et al. 2022). The early history and basic theory of coronal imaging, polarization measurement, and stray light rejection are covered by Billings (1966). More recently, “heliospheric imagers”, which work on the same principles as coronagraphs but observe farther from the Sun, have proved useful and require even deeper stray light rejection (e.g., Jackson 1985; Howard et al. 2008; Vourlidas et al. 2016; Howard et al. 2020; DeForest et al. 2022). The current generation of heliospheric imager uses imaging and stray-light rejection strategies similar those of coronagraphs, but typically in linear geometry rather than circular geometry.

Instruments to image the lower solar corona typically reject the solar light in an image plane: a low-scatter optic is used to develop an image of the Sun itself and the surrounding corona, and the solar light is either reflected/obstructed by an object at the focal plane (e.g., de Wijn et al. 2012), or allowed to exit the instrument through a hole in a mirror (e.g., Brueckner et al. 1995). This provides a sharp boundary on the image plane, separating photospheric light from coronal light without a wide vignetted boundary zone; but it also requires very low scatter in the first optic, which must minimize scattering of the bright photospheric beam into the much fainter coronal beam.

Because the coronal brightness drops off very rapidly, rejecting photospheric light from a focused image is not feasible for heliospheric imagers or for wide-field coronagraphs that view more than a fraction of a degree from the limb of the Sun itself. Solar coronagraphs viewing several solar radii from the Sun must reject stray light from the photosphere, by a factor smaller than 10^{-11} ; and wider angles require greater rejection. In this regime, external occultation is critical: the first optical element of the instrument is an occulting body that rejects the photospheric light via reflection or absorption, to separate it from the incoming beam before it can be scattered within the imaging system. The physics of diffraction around the occulter determine the performance of the instrument, and dominate the design of space instrumentation.

The basic theory of diffraction follows straightforwardly from the wave theory of light and is covered in common textbooks (e.g., Feynman et al. 1963; Hecht & Zajac 1974; Born & Wolf 1999); but a general treatment is intractable for analytic methods for all but the simplest cases. The two most famous simplified cases are Fraunhofer diffraction, in which the Born approximation holds and phase delays are considered to be linear in both incident angle and offset within the instrument; and Fresnel diffraction, in which phase delay is allowed to be quadratic in either incident angle or position. Although Fresnel diffraction is very useful in special cases, it is limited in its generality for occulter design, because many occulter solutions are three-dimensional objects and do not adapt well to the quadratic-phase-on-a-plane approach of the Fresnel approximation. Proper treatment of multiple vanes generally requires evaluating the Kirchoff integral (e.g., Born & Wolf 1999, Chap. 8) with little or no approximation, which in turn requires numerical evaluation/modeling; software tools used for this purpose include FRED (Photon Engineering 2021) and VirtualLab (LightTrans 2024). In practice, up to two-vane occulters are tractable for analytic treatment, but systems with three and more vanes are not (Aime 2020).

The problem of stray light rejection in a solar instrument is specific enough that general methods often do not apply straightforwardly. As a result, treatment of solar occulter systems is quite varied. Several studies have focused on performance of jagged or anti-aliased single occulters (Newkirk & Bohlin 1963; Fort et al. 1978; Lenskii 1981; Shirley & Datla 1996; Aime 2007); these may be treated with the Fresnel approximation and we do not consider them here. Round multi-disk external occulters have proved more tractable to fabricate and align, and have been incorporated in many prototype and actual instruments, from initial studies by Newkirk & Bohlin (1963), through the LASCO instruments (Brueckner et al. 1995; Bout et al. 2000), to the more modern STEREO/COR (Gong & Socker 2004), SOLO/METIS (Landini et al. 2012), ISS/CODEX (Yang et al. 2018), GOES/CCOR (Thernisien et al. 2021), and the ground-based CATEcor (DeForest et al. 2024). The design analysis methods for these instruments have been as varied as the occulters themselves, with a significant focus on highly simplified (e.g., Newkirk & Bohlin 1963), intuitive (e.g., Buffington 2000), empirical (e.g., Bout et al. 2000), and proprietary numerical (e.g., Gong & Socker 2004) methods. More recent work has explored the practical limits of analytic treatment (e.g., Aime 2020; Wang et al. 2021).

In considering design principles for future coronagraphs and heliospheric imagers, we sought to develop a middle ground: broadly applicable analytic design rules simpler to evaluate than the full Kirchoff integrals, which nevertheless provide both more rigor than intuitive empirical “horse sense”, and also well-defined limits of applicability. In this article, we develop from first principles a sufficient, simplified theory to understand and design externally occulted coronagraphs and heliospheric imagers, including why and how multi-edge occulters work in circular and linear geometry. We develop a 2-D approximation (successive-plane-wave approximation, SPW) for designing multi-edge occulters, derive from it the ideal geometry (cylindrical or ogive envelope) for a multi-edge system, and explore the limits of the SPW approach. As corollaries we derive both the root cause for the achromatic fringing seen around the occulters of existing externally occulted coronagraphs, and also the limits on performance of multi-edge occulters and their $n \rightarrow \infty$ limit, smooth occulters. The 2-D theory applies directly to extruded designs in 3-D, such as are used for contemporary heliospheric imagers (Howard et al. 2008; Vourlidis et al. 2016; Laurent et al. 2025); we also show how it applies to design of revolved designs in 3-D, such as in externally occulted coronagraphs.

Section 2 is an abbreviated derivation of the basic Fresnel attenuation formula to describe illumination inside the umbra of a sharp shadow mask (occulter). Section 3 develops the angular distribution of Fresnel-diffracted light around the edge, and shows the origin of the “bright ring” and “bright line” fringes that are seen in existing coronagraph and heliospheric imager data (e.g., Howard et al. 2008). Section 4 expands the theory to modern multi-edge occulters via an expedient approximation (the successive-plane-wave approximation), develops a design theory for curved-envelope multi-edge occulters, briefly touches on smooth occulters as a limiting case of multi-edge occulters, and discusses breakdown of the successive-plane-wave approximation. Section 5 develops a theory of multi-disk coronagraph occulters as a perturbation of the 2-D theory (which is also directly applicable to linear occulters as in heliospheric imagers).

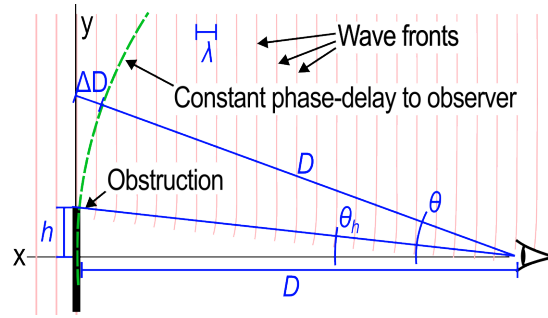


Figure 1. Fresnel scattering limits occulter performance. The most basic Fresnel calculation in 2-D involves plane waves incident on a simple occulting body. Constant-phase-delay surfaces around an observer at distance d from the body form circles on the plane. Each line of sight from the observer imposes a phase delay $\Delta D/\lambda$. In the Fresnel approximation, $\Delta D \propto \theta^2$.

Finally, in Section 6 we summarize the key points that develop from the theoretical discussion, and relate them to existing and future coronagraphs.

2. A QUICK REVIEW: 2-D FRESNEL DIFFRACTION AROUND AN EDGE

The Fresnel approximation to diffraction covers systems in which phase delay $\Delta\phi$ for the constituent paths of a diffracted wave is quadratically dependent on location in the scattering body; this contrasts with the even more common Fraunhofer/Born approximation, in which $\Delta\phi$ is linearly dependent on location. While treatments of Fresnel diffraction may be quite complex (and form the basis for photon sieves, Fresnel focusing optics, and holography), the simplest case (applicable to solar occulter) may be treated in 2-D (Figure 1). This essential 2-D treatment is directly applicable to heliospheric imagers, in which the system is extruded into the third dimension (e.g., Howard et al. 2008), and may be adapted to form a theory of externally occulted coronagraphs, in which the system is revolved around an axis of symmetry (e.g., Brueckner et al. 1995). While the problem of Fresnel diffraction around a simple occulting body is covered in some detail in standard optics textbooks (e.g., Born & Wolf 1999, , Chapters 8-11), it is worth an abbreviated treatment to establish terms and build immediate intuition.

Figure 1 sets up the essential geometry of the Fresnel diffraction problem around a simple occulter, which may be considered as an infinite half-plane extending into (and out of) the page in 3-D. The obstruction, of height h , is a distance D from the observer, and the locus of constant phase-delay from the incoming waves to the observer is a circle of radius D . Incident waves passing through the y axis below $y = h$ are truncated by the obstruction. Those above $y = h$ are subjected to a phase delay from the difference between the constant-phase-delay surface and the y axis. The additional distance ΔD results in a phase delay of $\Delta D/\lambda$ cycles (i.e. $2\pi\Delta D/\lambda$ radians). The wave fronts are taken to travel along the x direction, but without loss of generality as the angle of the obstruction relative to the wave fronts is unimportant to the problem.

The analysis is set up following Huygens' construction, replacing the incident plane wave with a line of oscillating sources along the y axis. Circular expanding wave fronts from each point on the axis interfere at the observer, with a phase delay that depends on the y coordinate and is determined by the distance ΔD normalized by the wavelength λ .

When considering Fraunhofer diffraction, for example in a single-slit or two-slit problem, one treats the constant phase-delay surface as piecewise flat, so that $\Delta D \propto y - y_0$ for some y_0 that fits the problem geometry. In the full wave treatment,

$$\Delta D = \sqrt{D^2 + y^2} - D, \quad (1)$$

which is analytically intractable. The Fresnel approximation expands the square root and keeps terms only up to y^2/D^2 (i.e. θ^2) approximation order, i.e.

$$\Delta D = D (y^2/2D^2 + \dots) \approx y^2/2D = D\theta^2/2. \quad (2)$$

With the approximation that $y \ll D$, projection polarization effects are negligible and light may be treated as a scalar wave (neglecting polarization and treating the electric field as a scalar quantity). Similarly, the radius $r \equiv \sqrt{y^2 + D^2}$ is independent of y in this regime and may be replaced with D , so that the $1/r$ dependence of the oscillating electric field on distance from a source may be neglected. Invoking Huygens' principle and replacing the oscillating electric

field of an incident wave with a matching collection of oscillating sources, we can follow Fresnel and immediately write:

$$E_{obs} = \frac{\phi E_0}{\sqrt{D\lambda}} \int_h^\infty e^{iy^2\pi/D\lambda} dy \quad (3)$$

where the (complex-valued) E_0 is the oscillating field at the y axis from the incoming plane wave, such that $E_0 E_0^* = I_0$, the incident intensity; ϕ is a constant complex phase-delay factor (i.e. $|\phi| = 1$) that is unimportant to the overall intensity; D and h are as shown in Figure 1; the $\sqrt{D\lambda}$ denominator normalizes for distance in the 2-D geometry and the required Huygens' wavelet normalization by λ (e.g., [Born & Wolf 1999](#), ch. 8); the integral is over all points on the y axis above the obstruction; the imaginary exponential tracks the phase delay introduced by ΔD at each value of y ; and λ is the wavelength of the incoming plane wave. Equation 3 is the Fresnel approximation to the oscillating electric field at the observer in Figure 1, due to equivalent source motion of a family of oscillating electric sources along the y axis to “mock up” the incident plane wave shown at left of Figure 1.

The integral in Equation 3 does not include a $1/r$ term, because $r \approx D$ when y is small, and the constant $1/D$ has been brought outside the integral. Integration to $+\infty$ breaks the $y \ll D$ approximation, but may be justified in two ways: analytically, by noting that in places where the approximation doesn't hold, the integrand oscillates very quickly, and therefore does not contribute significantly to the overall integral; and observationally, by noting that in real optical systems, occulter stray light is imaged mainly into a bright locus close to the occulter, i.e. where $y \ll D$ (Section 3). A more rigorous treatment of this approximation may be found in [Born & Wolf \(1999\)](#), Chapter 11. Making the jump from 2-D to 3-D involves either extrusion along the z (out-of-plane) axis for a linear baffle/occulter, or revolution about the x axis for a circular occulter. The first case is straightforward as z doesn't participate in Equation 3. The second requires some care and is discussed in Section 5.

The integral in Equation 3 can be simplified considerably. Picking the characteristic length

$$s \equiv \sqrt{D\lambda/\pi}, \quad (4)$$

and then defining a new variable u , such that $y = su$, yields

$$E_{obs} = \frac{\phi E_0}{\sqrt{\pi}} \int_{h/s}^\infty e^{iu^2} du. \quad (5)$$

The integral is transcendental and is described with the special functions

$$\mathcal{C}(\gamma) \equiv \int_0^\gamma \cos(u^2) du. \quad (6)$$

for the real part and

$$\mathcal{S}(\gamma) \equiv \int_0^\gamma \sin(u^2) du \quad (7)$$

for the imaginary part. Both functions are odd, and both approach the value $\pm\sqrt{\pi/8}$ as $\gamma \rightarrow \pm\infty$. Plotting them parametrically vs. γ on the complex plane yields the famous “Cornu spiral” in Figure 2, which graphically represents definite integrals of the form in Equation 5, without the scaling coefficients in front, and therefore forms a useful nomogram for evaluating integrals with the form of Equation 5. Important properties of the Cornu spiral include that its path length from the origin is equal to the γ parameter, that it slowly approaches limit points as $\gamma \rightarrow \pm\infty$, and that the local curvature of the spiral is proportional to γ . The curvature property was used in architecture and technical drawing throughout the pre-digital drafting era, in the form of the “French curve” templates that may be used to render smooth curves of arbitrary radius.

Writing the integral in terms of \mathcal{C} and \mathcal{S} puts a name to its solution, although the actual calculation of values on the Cornu spiral is typically via successive approximation. E_{obs} is given by

$$E_{obs} = \frac{\phi E_0}{\sqrt{\pi}} \left\{ \left[\sqrt{\pi/8} - \mathcal{C}(h/s) \right] + \left[\sqrt{\pi/8} - \mathcal{S}(h/s) \right] i \right\}, \quad (8)$$

and (remembering that $\phi^* \phi = 1$) the intensity I_{obs} at the observer is therefore

$$I_{obs} = I_0 \frac{1}{\pi} \left\{ \left[\sqrt{\pi/8} - \mathcal{C}(h/s) \right]^2 + \left[\sqrt{\pi/8} - \mathcal{S}(h/s) \right]^2 \right\}, \quad (9)$$

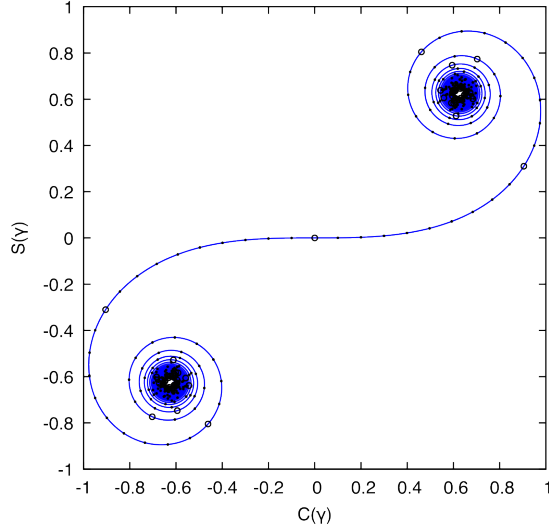


Figure 2. The Cornu spiral graphically represents the real and imaginary parts $\mathcal{C}(\gamma)$ and $\mathcal{S}(\gamma)$, respectively, of the Fresnel integral. The γ parameter is 0 at the origin. Integer values of γ are marked with small circles; every 0.1 is marked with a tick. The two asymptotes are at $\pm\sqrt{\pi/8}$ for both $\mathcal{C}(\gamma)$ and $\mathcal{S}(\gamma)$. A line drawn between two points on the spiral represents the complex Fresnel integral between the two corresponding values of γ , and its squared length is proportional to the corresponding intensity of light.

or, in terms of the angle θ_h and eliminating s ,

$$I_{obs} = I_0 \frac{1}{\pi} \left\{ \left[\sqrt{\pi/8} - \mathcal{C} \left(\theta_h \sqrt{D/\pi\lambda} \right) \right]^2 + \left[\sqrt{\pi/8} - \mathcal{S} \left(\theta_h \sqrt{D/\pi\lambda} \right) \right]^2 \right\}, \quad (10)$$

where θ_h is the bend angle of the light at the obstruction (as in Figure 1) and s is the characteristic length given by Equation 4.

Performing the Fresnel integrals is a matter of general interest and is relevant to many fields including radio-link engineering, holography, spectral and coded imaging, phase-shift imaging, and even cryptography. More prosaically, Equation 10 is useful for coronagraph design. It gives the total beam attenuation at a point in the umbra of a simple obstruction occulter from a monochromatic point source at infinity (collimated beam), given the wavelength of the light, distance from the occulter to the observer, and required bend angle of the beam to get around the edge of the occulter. The attenuation is plotted in Figure 3 for some example values of λ , D , and θ_h , and reproduces textbook half-plane attenuation formulae (Hecht & Zajac 1974; Born & Wolf 1999).

Although Equation 10 treats only a monochromatic beam and point source, one can integrate it numerically over angle and wavelength, to compute scattering attenuation from distributed and polychromatic sources. We discuss distributed sources, for the circular case only, in Section 5.

Exploring the limits of Equation 9 yields intuition. When $h \rightarrow -\infty$, the definite integral extends between the two asymptotes in Figure 2, and the expression collapses to $I_{obs} = I_0$ as it should with no obstruction present. When $h \rightarrow +\infty$, the definite integral extends from the positive infinity asymptote to itself, and the expression collapses to $I_{obs} = 0$ as it should when the beam is fully obstructed. When $h = 0$, $I_{obs} = I_0/4$, a famous result from Fresnel that helped (along with the presence of the Arago spot) to cement adoption of the wave theory of light (Arago 1819).

The form of the arguments to \mathcal{C} and \mathcal{S} in Equation 10 highlights a design constraint on physical geometry of occulters. For a given attenuation coefficient I_{obs}/I_0 ,

$$\theta_h \sqrt{D/\lambda} = k \quad (11)$$

where θ_h is the angle between the optics and occulter edge in a coronagraph, also called the “inner field of view cutoff” (Thernisien et al. 2005); and k is a constant that depends on the particular value of I_{obs}/I_0 . This is the essential design trade for externally occulted instruments: longer instruments can image closer to the Sun (by minimizing θ_h) – but doubling the length of the instrument only achieves a roughly 30% decrease in the required angular margin between the limb of the Sun and the inner field of view cutoff.

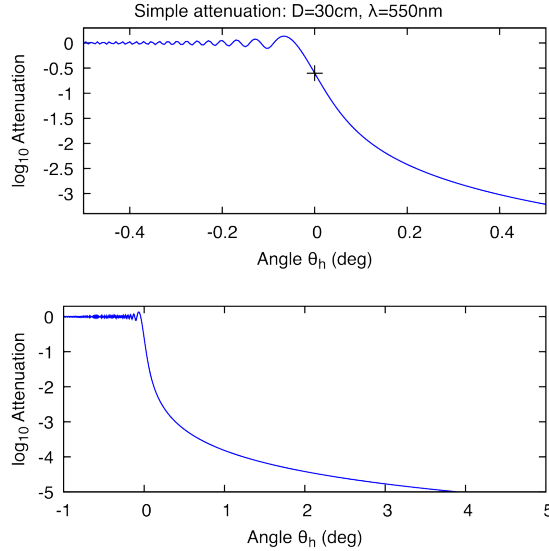


Figure 3. Attenuation from a sample single-edge occulter, calculated from Equation 10 for $\lambda=550\text{nm}$ and $D=250\text{mm}$, reveals the major aspects of Fresnel scatter by a half-plane: attenuation coefficient at $\theta_h=0$ is 0.25 (i.e. -0.6 on the \log_{10} scale) and is marked with “+”; high negative bend angles admit all light; low negative bend angles cause interference; and positive bend angles attenuate the light rapidly. Top plot shows attenuation close to the conventional edge of the occulter’s shadow. Bottom plot shows wider bend angles.

3. IMAGING FRESNEL-DIFFRACTED LIGHT

Coronagraphs and heliospheric imagers are imaging systems that resolve angle, so although an integral over the y axis (or equivalently θ) can predict the total amount of diffracted light entering the aperture, it cannot identify the diffraction features seen by a coronagraph or heliospheric imager. For that, it is necessary to fix θ (for a given pixel) and carry out the integral across the aperture instead of across incident angle. Figure 4 illustrates a simple imaging system with focal length F and aperture radius R . Light entering the aperture at angle θ is focused onto a focal point P behind the imaging system, a distance θF below the x axis.

At apparent locations (i.e. angles) far from the occulter, the imaging system works essentially independently of the occulter itself. But at angles close to the inner portion of the field of view, the aperture is vignetted by the occulter and the effective aperture of the instrument is reduced. This reduces total effective area of the instrument, and also affects the point-spread function due to conventional Fraunhofer diffraction through the reduced effective aperture [Lebaria et al. \(e.g., 2006\)](#). But the reduction of effective aperture size also affects the stray light pattern itself. Although straightforward models of coronagraph performance tend to reveal a “bright ring” around the occulter (e.g., [Rougeot et al. 2018](#)), real externally occulted coronagraphs exhibit diffraction fringes around the occulter, even when the optics are operated with broadband light. Some examples are shown in Figure 5.

To understand these imaged stray light features, one must consider more deeply the focusing system after the occulter. In Figure 4, the focusing system holds constant the phase delay between a given pixel on the detector and all the points on a flat (or, in the 2-D treatment, linear) “virtual slit” of width $W = 2R$ (with the same smallness condition as in Section 2, i.e. $y \ll D$ or equivalently $\theta \ll 1$). Because the virtual slit is canted (by θ) from the incident wavefronts and is small compared to the curvature of the constant phase surface to the aperture, the resulting intensity at P is subject to conventional Fraunhofer diffraction: there is an approximately linear relationship between incoming phase and position across the virtual slit. Revisiting the setup of Equation 3, with (for convenience) a square aperture $2R$ on a side,

$$E_P = \frac{\phi E_0 R}{DF\sqrt{\lambda}} \int_Q^R e^{i\frac{2\pi}{\lambda}\theta y'} dy', \quad (12)$$

where E_P is the computed electric field at Point P in Figure 5, ϕ is again an overall phase factor; E_0 is the incident wave electric field (treated as a scalar, as in Section 2); the D denominator arises from using the full 3-D geometry with linear extrusion of Figure 4 in the z direction (out of the page); a factor of R in the numerator accounts for the

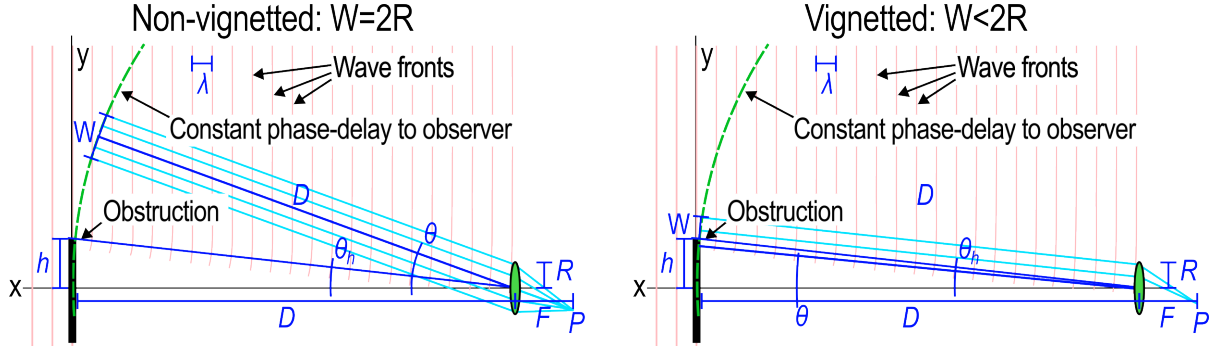


Figure 4. Geometry of an imaging system is different than that of a simple intensity sensor. The aperture of a focusing optical system forms a “virtual slit” of width W on the constant-phase surface of Figure 1, imposing a Fraunhofer diffraction pattern on the image plane. At wide angles (apparent distances) from the occulter (left panel), W is set by the entrance aperture and the Fraunhofer diffraction pattern takes the standard form in Equation 15. At narrow angles (apparent distances) close to the occulter (right panel), W depends on the relative geometry of the beam and the occulter, modifying the functional form as in Equation 22.

aperture integral in the z direction, over which the integrand is constant; F is the focal length of the optics; dy' is a perturbative variable of integration around y (i.e. centered on $D\theta$); and the lower limit of integration, Q , is the greater of $-R$ and $(D\theta - R) - h$. The integral is just the Fourier transform of the rectangular function from Q to R ,

$$E_P = \frac{\phi E_0 R \sqrt{\lambda}}{i 2\pi \theta D F} \left[e^{i \frac{2\pi}{\lambda} \theta y'} \right]_{y'=Q}^R. \quad (13)$$

In the far (unvignetted) field, $Q = -R$ and Equation 13 devolves to the familiar single-slit diffraction formula for the E-field at a non-vignetted focal plane point P_{nv} :

$$E_{P_{nv}} = \frac{\phi E_0 R \sqrt{\lambda}}{\pi \theta D F} \sin \left(\frac{2\pi}{\lambda} \theta R \right), \quad (14)$$

with the corresponding intensity

$$I_{P_{nv}} = I_0 \frac{R^2 \lambda}{\pi^2 \theta^2 D^2 F^2} \sin^2 \left(\frac{2\pi}{\lambda} \theta R \right). \quad (15)$$

Equation 15 is just the usual wide-slit Fraunhofer formula – a squared sinc function in θ – that is scaled to the specific geometry of the $2R \times 2R$ aperture and focal length of the optics, giving the intensity $I_{P_{nv}}$ at each location in the focal plane. $I_{P_{nv}}$ has zeroes at

$$\theta = \frac{n\lambda}{2R} \quad (16)$$

for every $n \in \mathbb{Z}^+$, so that each peak is half the width of the conventional diffraction limit around the $n = 0$ peak. Given that n is large across the image, and that most instruments are at least somewhat polychromatic, the oscillating factor disappears in a typical instrument, and we are left with a locally smoothed stray light intensity $\bar{I}_{P_{nv}}$:

$$\bar{I}_{P_{nv}} = I_0 \frac{R^2 \lambda}{2\pi^2 \theta^2 D^2 F^2}, \quad (17)$$

which describes a smooth stray light pattern extending across the field of view and varying as θ^{-2} and λ .

Where $D\theta < h + R$, the beam intersects the occulter vane and $Q \neq -R$. In that portion of the field of view, the cosine terms implicit in Equation 13 don't cancel directly as in Equation 14. But, recognizing the system's symmetry under displacement, we can adopt new symmetric limits by re-centering the coordinate system on the slit, and the cost of adopting fixed phase delay. Setting θ_0 to be the lowest angle at which any ray can enter any part of the square aperture,

$$\theta_0 \equiv \frac{h - R}{D}, \quad (18)$$

and one can re-center using an equivalent-radius R' . Defining :

$$R' \equiv (\theta - \theta_0)D/2. \quad (19)$$

Then, at vignetted points Pv ,

$$E_{Pv} = \frac{\phi\psi E_0 R\sqrt{\lambda}}{\pi\theta DF} \sin\left(\frac{2\pi}{\lambda}\theta R'\right), \quad (20)$$

where, compared to Equation 15, the ψ is another phase-delay factor, the numerator factor of R remains the same because it is associated with the z integral, and the limits of integration in the y' direction are now $\pm R'$ relative to the center of the vignetted effective slit. Equation 20 differs subtly but importantly from 15 in that R' is θ -dependent. Expanding R' and defining $\Delta\theta \equiv \theta - \theta_0$,

$$E_{Pv} = \frac{\phi\psi E_0 R\sqrt{\lambda}}{\pi\theta D} \sin\left(\frac{\pi DF}{\lambda} \{\Delta\theta^2 + \theta_0\Delta\theta\}\right), \quad (21)$$

with corresponding intensity

$$I_{Pv} = I_0 \frac{R^2\lambda}{\pi^2\theta^2 D^2 F^2} \sin^2\left(\frac{\pi D}{\lambda} \{\Delta\theta^2 + \theta_0\Delta\theta\}\right). \quad (22)$$

The argument of \sin^2 is quadratic, rather than linear, in $\Delta\theta$; this has the effect of changing the oscillation frequency of the sinc function near the occulter. In particular, zeroes occur for every $n \in \mathbb{Z}^+$ where

$$\Delta\theta^2 + \theta_0\Delta\theta - n\frac{\lambda}{D} = 0, \quad (23)$$

or

$$\Delta\theta = \frac{\theta_0}{2} \left(\sqrt{1 + 4n\lambda/D\theta_0^2} - 1 \right), \quad (24)$$

where the negative branch of the square root is unphysical. If n is small and the bend angle θ_0 is large compared to λ/D , then $n\lambda/D\theta_0^2 \ll 1$; in that case Equation 24 reduces to

$$\Delta\theta = \frac{n\lambda}{D\theta_0}, \quad (25)$$

so that individual dark fringes in the large-bend-angle regime follow the conventional Fraunhofer diffraction formula and are found at $\Delta\theta$ angles of

$$\Delta\theta_n - \Delta\theta_{n-1} = \frac{\lambda}{D\theta_0}. \quad (26)$$

Contrariwise, if n is sufficiently large or the bend angle θ_0 is small, then $n\lambda/D\theta_0^2 \gg 1$ and in this small-bend-angle regime, Equation 24 reduces instead to

$$\Delta\theta = \sqrt{\frac{n\lambda}{D}}, \quad (27)$$

so that individual fringes have width that varies as

$$\Delta\theta_n - \Delta\theta_{n-1} \approx \sqrt{\lambda/Dn} \quad (28)$$

until the unvignetted condition is reached. Which of Equation 25 or 28 is important to the observed pattern near an occulter in a real single-occulter instrument depends on the interplay between θ_0 , D , and λ , but in general if θ_0 is comparable to or smaller than the conventional diffraction limit of the optics, then Equation 28 applies. In that case, the fringe pattern depends only on D and (weakly) on λ , not on the specific geometry of the occulter itself.

In Section 4, we discuss multiple-edge occulters. In a multiple-edge system, the important scattering angle θ_0 can be quite small at the last stage of occultation, and Equation 28 therefore drives the appearance of the occulter edge. For example, in a spaceborne coronagraph operating at $\lambda=650$ nm, with $D=250$ mm, and a final scattering angle of $\theta_0=1.25'$, $\lambda/D = 2.6 \times 10^{-6}$ and $\theta_0^2 = 1.4 \times 10^{-7}$, so Equation 28 applies, and the innermost ‘‘bright ring’’ fringe around the occulter is approximately $5.1'$ wide. Because the width of the fringe depends only weakly on λ , varying the wavelength over a wide range of 450-650 nm would incur only a 20% shift in the width of the first few fringes, which will therefore appear nearly achromatic.

Figure 5 shows four examples from real instruments of the quasi-achromatic fringing effect described by Equation 28. SOHO/LASCO-C2 uses a hybrid occultation scheme and therefore the innermost bright fringe is obscured by the

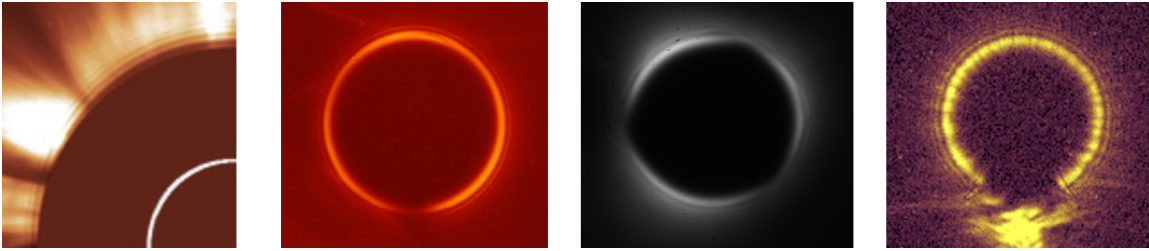


Figure 5. Quasi-achromatic fringing is characteristic of external occultation as seen with four separate externally occulted instruments. Each image shows fringing around the image of the external occulter in the focal plane, following Equation 28. (A) SOHO/LASCO C2 (Brueckner et al. 1995), though the lowest order fringes are obscured by C2’s internal occulter; (B) A conical occulter under test (Yang et al. 2018); (C) CATEcor (DeForest et al. 2024), (D) SwSCOR (Erickson et al. 2025). The LASCO image is zoomed in to reveal the high-order fringes from the external occulter, as seen around the internal occulter.

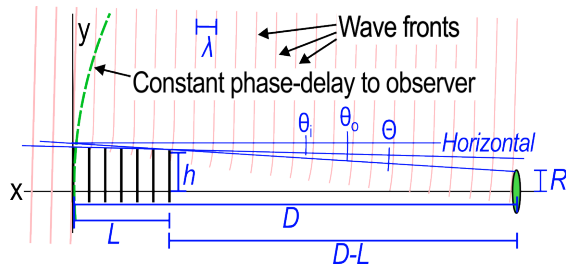


Figure 6. A basic multi-edge occulter geometry in 2-D is applicable to linear heliospheric imagers (via extrusion along the z axis, out of the page) or externally occulted coronagraphs (via revolution about the x axis). Light incident from θ_i above the horizontal is scattered off multiple edges along an occulter of length L , exiting at θ_o to barely graze the edge of an optical entrance aperture. The occulter requires the light to bend by at least Θ to enter the aperture.

internal occulter and only higher order fringes are visible at the inner occulted edge; it “should be” surprising that any fringes are visible at all, given that LASCO C2 is a broadband white-light instrument (Brueckner et al. 1995). The other three images, from multiple test-article occulters, highlight the characteristic extra-wide first fringe and more rapid subsequent fringes described by Equation 28.

Equation 28 thus explains the quasi-achromatic fringes seen with existing externally occulted coronagraphs. The spacing of the fringes is seen to be approximately independent of the occulter geometry itself, and to depend primarily on the length of the instrument between the occulter and imaging aperture. The fringe spacing depends only weakly on wavelength, allowing even broadband instruments such as LASCO/C2 (Brueckner et al. 1995) or CATEcor (DeForest et al. 2024), with $\lambda/\Delta\lambda < 3$, to show visible fringes up to $n = 6$ or more, when a naïve consideration might expect $n = 3$ at most.

4. MULTI-EDGE SCATTERING

Section 2 described the case of 2-D scattering around a single edge. In practice, modern occulters use a multi-edge structure, and many multi-disk geometries have been tried, including two- and three-disk occulters (Brueckner et al. 1995), conical multi-disk occulters (Brueckner et al. 1995; Landini et al. 2012; Yang et al. 2018), and even smooth occulters as a limiting case of “infinite” disk count (Buffington 2000; Bout et al. 2000). We note that, because the attenuation drops fastest at low values of θ_h (as seen in Figure 3), many edges (with small angular offset each) attenuate light faster than fewer edges (with a larger angular offset each). This effect was described by Newkirk & Bohlin (1963), and exploited in the three-disk occulter of the “C3” and 160-disk conical occulter of the “C2” instruments in the Large Angle Spectroscopic COronagraph (LASCO) instrument (Brueckner et al. 1995). It has since become a common element of occulter design in subsequent spaceborne instruments (Howard et al. 2008; Yang et al. 2018; DeForest et al. 2022; Dudley et al. 2023).

In the general case, calculating the scattering around multiple occulter edges is complicated enough to violate the Fresnel diffraction conditions, requiring direct evaluation of the more complicated Kirchoff integral. In practice, a straightforward “rough-and-ready” approach is sufficient to develop intuition and establish a working design.

The successive-plane-wave (SPW) approximation is such an approach: Fresnel diffracted light from each edge in a multi-edge occulter is considered to approximate a plane wave when it encounters the next edge. This is a reasonable approximation, because in practice multi-edge occulters are in the regime described by Equation 28 and therefore the illuminating beam for a given edge arises from a space slightly above the prior edge and nearly parallel to the line (in the 2-D treatment) formed by the tops of the two edges. SPW puts a name and formal framework to an approximation that has already been used, without strong justification in the literature, for multi-vane occulters in circular and linear geometry (e.g., Buffington et al. 1998; Thernisien et al. 2018).

The SPW treatment immediately enables a simple optimization of occulter shape design, by treating the overall multi-edge occulter as an independent sequence of individual scatters, each of which follows Equation 10 for a small bend angle $\Delta\Theta$ and radius equal to the inter-disk spacing. We immediately observe that, because the single-edge attenuation is nonlinear, becoming more shallow with angle (e.g., Figure 3), dividing offset angle equally between all active edges in a multi-edge occulter optimizes the overall effectiveness.

Equipartition of angle across edges is optimal because, given two equally-spaced vanes a and b with different $\Delta\Theta_a$ and $\Delta\Theta_b$, and having individual attenuation coefficients A_a and A_b as given by Equation 10, if (without loss of generality) $\Delta\Theta_a < \Delta\Theta_b$, then (from Equation 10 and as illustrated in Figure 3), $-d(\log A_a)/d\Theta_a > -d(\log A_b)/d\Theta_b$, and it is beneficial to grow Θ_a at the expense of Θ_b , holding the sum constant, in the sense that doing so improves the overall attenuation of both acting together. Therefore, a valid way to design a multi-edge occulter for a particular bend angle Θ is to start with a single-edge design, then expand the occulter into a collection, with overall length L , of n edges spaced equally along the beam direction, $\Delta L \equiv L/n$ apart and having bend angle $\Delta\Theta \equiv \Theta/n$ each, as in Figure 6. Designs created this way have edges aligned along circular envelopes in 2-D, or either cylindrical or ogive¹ envelopes in 3-D for heliospheric imagers or coronagraphs, respectively. They therefore provide more engagement of each individual vane with the propagating wavefronts, than do conical occulters (e.g., Bout et al. 2000; Landini et al. 2012; Baccani et al. 2016; Aime 2020).

The same 2-D analysis is also applicable to toroidal corral baffles such as those developed by Buffington (2000), as toroidal corrals are formed by revolution around a line parallel to the y axis and displaced in the $+x$ direction, in Figure 6.

In the SPW treatment, Equation 10 becomes

$$I_{obs} = I_0 \left[\mathcal{M} \left(\Delta\Theta \sqrt{\pi \Delta L / \lambda} \right) \right]^{n-1} \mathcal{M} \left(\Delta\Theta \sqrt{\pi (D - L) / \lambda} \right), \quad (29)$$

where the auxiliary function \mathcal{M} is just the complicated part of Equation 10:

$$\mathcal{M}(\gamma) \equiv \frac{1}{\pi} \left\{ \left[\sqrt{\pi/8} - \mathcal{C}(\gamma) \right]^2 + \left[\sqrt{\pi/8} - \mathcal{S}(\gamma) \right]^2 \right\}. \quad (30)$$

The first $n - 1$ coefficients in Equation 29 represent scatters by the first $n - 1$ disks; the last term is broken out because the scatter is over the generally-much-longer distance all the way to the focusing optics. In Equation 30, \mathcal{M} takes the form of an analytic propagator for edge scattering, and is a simpler form than the propagator derived by Wang et al. (2021) through more rigorous analysis.

Equation 29 is computable but complicated. More simplification is possible, to reveal the essential behavior of the propagator. For a typical solar occulter, $\Delta\Theta$ might be on the order of 1-2 arcmin, and ΔL might be on the order of 5 mm. For those numbers and a wavelength of 650 nm, the argument to \mathcal{M} evaluates to 0.05–0.1. That affords the approximations

$$\mathcal{C}(\gamma) \approx \gamma \quad (31)$$

and

$$\mathcal{S}(\gamma) \approx 0, \quad (32)$$

which may be verified from their definitions in Equations 6 and 7 when γ is small. In turn, that yields

$$\mathcal{M}(\gamma) \approx \frac{1}{\pi} \left\{ \left[\sqrt{\pi/8} - \gamma \right]^2 + \pi/8 \right\} \approx \frac{1}{\pi} \left\{ \frac{\pi}{4} - 2\gamma \right\} = \frac{1}{4} \left[1 - \frac{8\gamma}{\pi} \right] \quad (33)$$

¹ Readers are reminded that an *ogive* is a figure of revolution of a circle or section of a circle, about a non-diameter chord of that circle. While a cone or frustum has zero curvature along the axial direction, an ogive has constant curvature along the axial direction.

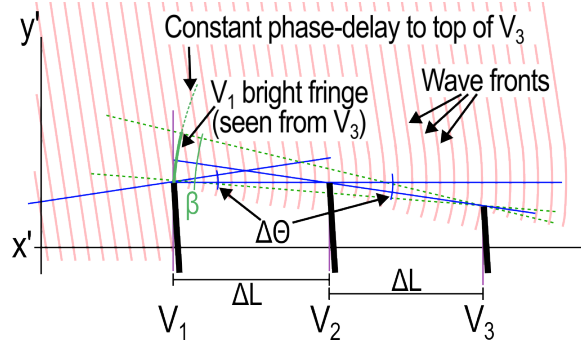


Figure 7. Close-up rendering of the geometry in Figure 6 illustrates a limit of the successive plane wave (SPW) approximation, using a hybrid ray approach. As ΔL and/or $\Delta\Theta$ shrink, V_2 fails to fully obscure rays from the first bright fringe above V_1 , as seen from the top of V_3 . Note the tilted (x', y') frame of reference, selected to make V_1 – V_2 horizontal on the figure.

for those coefficients. Equation 29 thus simplifies to

$$I_{obs} \approx I_0 \left[\frac{1}{4} \left(1 - 8\Delta\Theta \sqrt{\frac{\Delta L}{\pi\lambda}} \right) \right]^{n-1} \mathcal{M} \left(\Delta\Theta \sqrt{\frac{\pi(D-L)}{\lambda}} \right). \quad (34)$$

Equation 34 points intuitively to the reason why conical coronagraph occulter (e.g., Bout et al. 2000; Landini et al. 2012, 2017) work. In the ray approximation, a conical multi-disk occulter “should” yield no improvement over a dual-disk occulter, because the intermediate disks don’t intersect any rays. But the intermediate disks do interact with wave fronts and further attenuate stray light that, in the ray approximation, would merely graze across the top of each disk in the conical assembly. So long as the SPW approximation is valid, this yields a minimum attenuation of a factor of 4 per disk (or vane in a linear occulter).

In a circular-profile design, each disk attenuates slightly more than a factor of 4, because of the perturbation coefficient in parentheses, inside the square brackets of Equation 34. In the specific case of $n = 10$, $\Delta L = 5\text{mm}$, $\Delta\Theta = 1.5'$, and $\lambda = 650\text{nm}$, the perturbation coefficient evaluates to 0.83, improving the total attenuation by nearly an order of magnitude. But as n increases (at constant L and Θ), both $\Delta\Theta$ and ΔL decrease, and the perturbation coefficient rapidly approaches unity. In the large- n case that coefficient may be neglected entirely, yielding

$$\lim_{n \rightarrow \infty} I_{obs} = I_0 (1/4)^n. \quad (35)$$

This large- n case has been described by several authors, with varying degrees of analytic rigor, since the mid 20th Century (Newkirk & Bohlin 1963). Equations 34 and 35 represent a middle way between intuitive observation (Buffington et al. 1998) and more recent detailed analytic treatments (Wang et al. 2021) that reveal similar results through rigorous analysis followed by formal approximation.

Because Equation 35 predicts much better performance for multi-edge occulter as n increases, which is not borne out in the “infinite-edge” case of smooth occulter (e.g, Bout et al. 2000), it is useful to explore the practical limits on n . Mechanical tolerance is one limit: in the same hypothetical case as above, with $n = 10$, $\Delta L = 5\text{mm}$, $\Delta\Theta = 1.5'$, and $\lambda = 650\text{nm}$, the edges must have h placement precision (including both fabrication and alignment errors) of $\pm 2 \mu\text{m}$ to ensure all edges interact with the beam; and adding more edges (within the same length) tightens the positional tolerance according to n^{-2} . Indeed, this effect was thought to be the reason that Newkirk & Bohlin (1963) did not observe the theoretical benefit when they fabricated, assembled, and tested a 140-disk occulter made from individual graduated disks on a spindle.

But, surprisingly, mechanical tolerance is not necessarily the limiting factor for n : the SPW approximation itself fails at high n . Smooth occulter, which represent the $n \rightarrow \infty$ limit, are not infinitely effective. To find the limits of SPW, we explore its breakdown in two different ways: via a hybrid ray-diffraction approach, and via analysis of how wavefronts at each edge change from simple plane-waves (or even constant-radius wave fronts) as n increases.

4.1. Limits of the SPW approximation: hybrid approach

Figure 7 is a close-up rendering of a portion of the occulter in Figure 6, showing two approaches to understanding the breakdown of SPW. Three vanes, separated by ΔL in space and $\Delta\Theta$ in angle, form part of an occulter with cylindrical

(in extruded linear geometry) or ogive (in revolved circular geometry) overall envelope. For convenience, the x and y directions are replaced with x' and y' , rotated so that the V_1 – V_2 direction is along the x' axis. Incident plane waves arrive at V_1 rising at an angle $\Delta\Theta$ and interact with the edge. The V_2 – V_3 direction drops by $\Delta\Theta$ relative to V_1 – V_2 .

In the ray approximation, V_2 in Figure 7 is high enough to prevent rays from V_1 from reaching V_3 . However, diffracted light that passes over V_1 to reach V_3 actually passes mainly through the space just above V_1 . That space is approximated by the locus, pictured in the left panel of Figure 7 and labeled “ V_1 bright edge”, where the Fresnel integrand u in Equations 6 and 7 varies by roughly unity, i.e. from near 0 to less than 1. That approximation holds because, in the case under consideration, the h/s value for V_1 itself, relative to V_3 , is close to zero, and the first unit of range in the \mathcal{C} and \mathcal{S} integrations contributes most strongly to the total value of the Fresnel integrals in Equation 10. That effect is related to, but not the same as, the fringing discussed in Section 3: that fringing requires interaction between an aperture and an occulter edge, while this effect has to do with the locations on the y' axis that contribute most strongly to the Fresnel integrals. If that locus is directly visible from the top of V_3 , the edges do not act independently and the SPW approximation becomes invalid. Thus the SPW treatment requires at least

$$\beta < \Delta\Theta, \quad (36)$$

where β is labeled in Figure 7, and is given by

$$\beta = \frac{h'}{2\Delta L} \quad (37)$$

and

$$h' = s \equiv \sqrt{2\Delta L\lambda/\pi}, \quad (38)$$

where h' is height above V_1 and s is calculated (using Equation 4) for the V_1 – V_3 gap in the absence of V_2 . So the overall requirement for the successive-plane-wave approximation is

$$\Delta\Theta > \frac{\sqrt{2\Delta L\lambda/\pi}}{2\Delta L} = \sqrt{\frac{\lambda}{2\pi\Delta L}} \quad (39)$$

Equation 39 can be reduced further, by noting that in an n -edge occulter of length L , $\Delta\Theta = \Theta/n$ and $\Delta L = L/n$, to arrive at a limiting n for given occulter parameters:

$$\Theta/n > \sqrt{\frac{n\lambda}{2\pi L}} \quad (40)$$

or, solving for n ,

$$n < \left(\frac{2\pi\Theta^2 L}{\lambda}\right)^{1/3}. \quad (41)$$

For example, for an occulter with $\Theta = 0.5^\circ$ and $L = 75$ mm operating at 650 nm, the maximum n is roughly 4. At higher n , one might expect occulter performance to diverge from the SPW model, becoming worse because each vane no longer obscures the bright edge of the prior vane, from the successive vane. However, SPW-based calculations have proven to be good estimators of occulter performance in multiple geometries even when Equation 41 implies they should not (Laurent et al. 2025; Erickson et al. 2025). Understanding why requires a slightly less facile treatment, which we explore in the next section.

4.2. Limits of the SPW approximation: spliced-wavefront approach

Full treatment of a multi-edge system requires evaluating the complete Kirchoff diffraction integral (Born & Wolf 1999, Chap. 8), of which the Fresnel integral (Equation 3) is but an approximation. Many authors discuss the use of numerical methods to evaluate that integral (e.g., Breault 1977; Gong & Socker 2004; Yang et al. 2018). But it is possible to understand the limits and form of SPW violation even without resorting to numerical methods, by considering the way in which the wavefronts begin to violate the conditions for both the SPW and Fresnel approximations as n increases.

Wavefront shape evolves in two important ways as n increases (at constant L). The first is illustrated at the V_2 edge in Figure 8. The wave fronts arriving at the V_2 edge from V_1 are not actually planar, and can each be better approximated with (in 2-D) a circular segment of radius ΔL , spliced to a plane-wave segment that is perturbed only

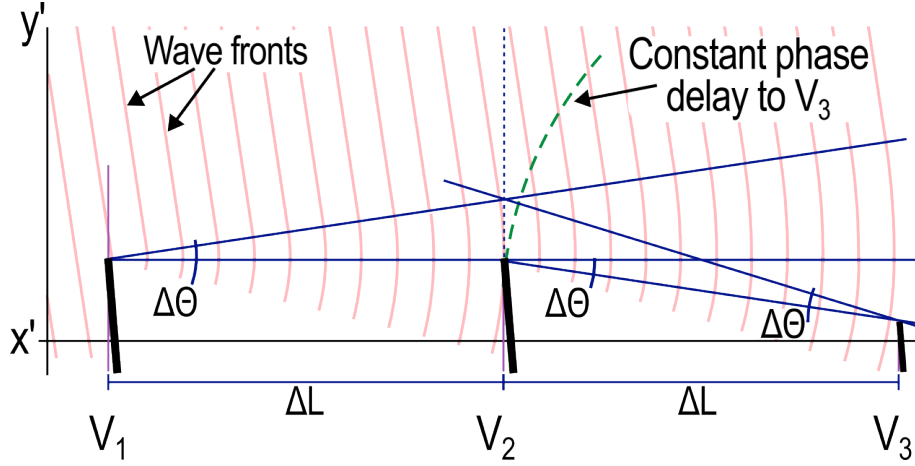


Figure 8. A second close-up rendering of the geometry in Figure 6 recaps Figure 7 from a wavefront perspective. Following Huygens' principle, perturbed wavefronts may be approximated (in 2-D) by splicing a circular arc onto the unperturbed part of the wave front. Taking the Huygens' wavelet approach along the dotted line above V_2 thus yields two Fresnel integrals: one for the portion of the wavefront that is perturbed by V_1 (and therefore curves with radius ΔL), and one for the unperturbed, straight portion of each wavefront. For convenience the incident angle onto V_1 is taken to be the same as $\Delta\theta$ for each vane of the occulter as a whole. The (x', y') axes are selected to make the $V_1 - V_2$ line horizontal, which makes the vanes themselves appear slanted.

negligibly by the interaction with V_1 . The SPW approximation treats this approximately circular segment of the wavefront at V_2 (and subsequent vanes) as negligible to the overall shape of the wavefronts as they propagate along the occulter.

While the exact shape of the wavefront at V_2 is complicated to describe analytically, it is straightforward to approximate it by simply splicing a circular and linear segment together. For the case of V_2 , Equation 5 breaks into two integrals. E_3 , the electric field at the top of V_3 in Figure 8, can be written

$$E_3 = \frac{\phi}{\sqrt{\pi}} \left(\int_{\epsilon}^{2\epsilon} E_2(u) e^{i2u^2} du + e^{i2\epsilon^2} \int_{2\epsilon}^{\infty} E_2(u) e^{iu^2} du \right), \quad (42)$$

where

$$\epsilon \equiv \Delta L \Delta\theta / s = \Delta\theta \sqrt{\frac{\Delta L \pi}{\lambda}}, \quad (43)$$

and the function $E_2(u)$ is the calculated electric field at each location along the line of integration above V_2 . $E_2(u)$ may be calculated directly using Equation 5 applied to an observer at the corresponding location above V_2 , due to Fresnel diffraction effects imposed by V_1 and the incident plane waves. The initial factor in Equation 42 is the same as in Equation 5.

The first integral of Equation 42 describes the contribution to E_3 from space between the top of V_2 (which is elevated above the direct line of sight from V_3 to V_1 by the distance $\Delta\theta L$) to the top of the spliced circular approximate wavefront (which is $\Delta\theta L$ higher still). The imaginary exponent in the integrand has a $2u^2$ term describing the doubled curvature from the two circular constant-phase surfaces: one from V_1 and one to V_3 . It also has a linear term describing the opening angle between the two constant-phase surfaces, which is $\Delta\theta$ at the top of V_2 .

The second integral of Equation 42 describes the contribution to E_3 from the space above the top of the spliced circular wavefronts, where the wavefronts are approximated with straight lines. The quadratic term is dependent only on u^2 and not on $2u^2$, accounting for the single curvature of the constant phase-delay surface to V_3 from the line of integration. The imaginary exponential term in front of the integral matches the phase delay at the splice point between the linear and circular approximations.

Cleaning up the integration with another substitution $u = v/\sqrt{2}$,

$$E_3 = \frac{\phi}{\sqrt{\pi}} \left(\frac{1}{\sqrt{2}} \int_{\sqrt{2}\epsilon}^{2\sqrt{2}\epsilon} E_2(v/\sqrt{2}) e^{iv^2} dv + e^{i2\epsilon^2} \int_{2\epsilon}^{\infty} E_2(u) e^{iu^2} du \right). \quad (44)$$

Calculating E_3 with Equation 42 or 44 is complicated in the general case. However, we are not interested in the general case, but in the case where $\Delta\Theta$ is small and where ΔL is at most comparable to s . Following the example of Fresnel himself, we can therefore simplify Equation 42 by aggressively approximating and/or neglecting effects wherever possible.

In particular, $\epsilon \ll 1$ and therefore Equations 31 and 32 hold, which simplifies the problem considerably. Further, we can approximate E_2 as piecewise constant in u . In the linear regime we set ${}^{|}E_2(u) = E_0$, and in the circular regime, we allow ${}^{\circ}E_2$ to be attenuated by the constant attenuation term for Fresnel diffraction around V_1 onto the edge of V_2 (where the $|$ and \circ mark which regime is being used for the calculation). Applying the relevant geometry to Equation 8, and applying Equations 31 and 32, yields

$${}^{\circ}E_2 = \phi' E_0 \left\{ \frac{1}{2} - \frac{1}{\sqrt{\pi}} \epsilon \right\}, \quad (45)$$

where ϕ' is a phase factor approximately equal to $e^{i\pi/4}$.

Substituting for ${}^{|}E_2$ and ${}^{\circ}E_2$, neglecting two small phase shifts, and using Equations 31 and 32 both evaluates the integrals from Equation 44 and simplifies the remaining terms:

$$E_3 = \frac{\phi'' E_0}{\sqrt{\pi}} \left(\left(\frac{1}{2} - \frac{\epsilon}{\sqrt{\pi}} \right) \epsilon + \sqrt{\pi} \left(\frac{1}{2} - \frac{\sqrt{2}}{\sqrt{\pi}} \epsilon \right) \right), \quad (46)$$

where ϕ'' rolls up the phase shifts. Equation 46 simplifies further, to

$$E_3 = \phi'' E_0 \left(\frac{1}{2} - \frac{1 + \sqrt{2\pi}}{\pi} \epsilon - \frac{1}{\pi} \epsilon^2 \right). \quad (47)$$

Equation 47 yields a separate estimate, independent of Equation 40, of when and how the SPW model breaks down at low values of ΔL and/or $\Delta\Theta$. In particular, SPW predicts (Equation 33) that the combined effect of V_1 and V_2 on the illumination at V_3 should be an overall attenuation of better than 1/4 in E (or, equivalently, 1/16 in I). That relation only holds if

$$\epsilon > 0.22\dots \quad (48)$$

Expanding ϵ (via Equation 43) and solving for n as in the derivation of Equation 41,

$$n < \left(\frac{20\pi\Theta^2 L}{\lambda} \right)^{1/3}, \quad (49)$$

which is considerably less stringent than Equation 41. For the same occulter parameters as considered in Section 4.1, the spliced wavefront approach predicts agreement with SPW for occulters with at least 8 vanes.

Examining the wavefronts at right in Figure 8 reveals that, at high n , the two-wavefront splicing approach that led to Equations 42 – 47 is pessimistic about the overall attenuation of multi-vane occulters. There are two reasons for that pessimism.

Firstly, in calculating E_3 we treated the strength of the linear section of the wave fronts as equal to the incident field strength, but this is not the case. In particular, the nomogram in Figure 2 and the demonstration attenuation plots in Figure 3 show that the incident wavefronts at V_2 are attenuated significantly at small negative values of ϵ (or equivalently, h), i.e. in exactly the portion of the linear wavefront segment that contributes most strongly to the intensity at V_3 . The approximation makes the integrals in Equation 44 far more tractable by forcing them into the same form as in Equation 5, but also makes Equation 49 pessimistic by a factor of order $2^{1/3}$.

Secondly, wavefronts near successive vanes are further modified by each prior vane, beyond the simple two-segment splice we described. In Figure 8, the wavefront over V_3 is better described by three segments with piecewise-constant curvature: the lowest portion is formed by the last few Huygens' wavelets just above V_2 , and has radius ΔL . The middle portion is formed around V_1 and has radius $2\Delta L$. As the wavefronts propagate along the occulter to subsequent vanes, more splices are required; and the effect is to cause occulters with large n to attenuate slightly more than the subsequent simple splices suggest.

These two effects suggest that the regime of SPW applicability is best approximated with the formula

$$n_{max} \sim \left(\frac{50\pi\Theta^2 L}{\lambda} \right)^{1/3}, \quad (50)$$

where the factor of 50 arises from a combination of the $2^{1/3}$ from the $^{\circ}E$ attenuation and a small correction for the multiple-radius curve in $^{\circ}E$. Equation 50 implies a practical maximum of 11-12 vanes for the example occulter described above, before performance begins to fade below the SPW prediction, and further explains why smooth occulters perform only marginally, and not infinitely, better than multi-vane occulters even under ideal conditions.

5. DISK OCCULTERS

Coronagraph external occulters are typically circular. Revolving the system of Figure 1 about the x axis yields a typical coronagraph geometry, with one or a series of disk edges blocking sunlight from entering the instrument. In general, the geometry is set such that the final exit angle θ_0 from the occulter (visible in Figure 6) becomes the cone angle of a “shadow frustum” whose large end, at the rear of the occulter, has radius h and whose small end, at the entrance aperture, has radius R , slightly larger than the entrance aperture of the optics. θ_i is tuned to be slightly larger than the apparent size of the Sun.

Many aspects of coronagraph design are agnostic to whether the occulters of Figures 1,4, and 6 are extruded along the third dimension (as in a linear-geometry heliospheric imager) or revolved about the x axis (as in a circular-geometry coronagraph), with two important exceptions.

The first important feature of revolved (cylindrical, conic, or ogive) occulters is in the angular image domain: brightness of the fringes discussed in Section 3 scales inversely as the apparent distance ε from the boresight of the instrument. In this geometry, Equation 17 becomes

$$^{\circ}\bar{I}_{Pnv} = I_0 \frac{R^2 \lambda}{2\pi^2 F^2 (\varepsilon - \varepsilon_{min})^2 \varepsilon D^2}, \quad (51)$$

where $^{\circ}\bar{I}_{Pnv}$ is the average brightness of the fringes in the circular geometry, ε_{min} is the apparent size of the inner field-of-view cutoff of the detector, and (as in Equation 17) $^{\circ}\bar{I}_{Pnv}$ is calculated as a deposited power per unit area at the focal plane and thus depends on the focal length of the optics, F . The additional factor of ε^{-1} arises because, as apparent distance from the centerline increases, the light from a given small length of occulter edge is spread across more of the focal plane. Furthermore, far from the apparent edge of the occulter, ε_{min} is negligible and $^{\circ}\bar{I}_{Pnv}$ drops off as ε^{-3} ; this form matches the known dropoff rate of the coronal brightness (e.g., DeForest et al. 2016), ensuring that diffracted stray light does not dominate the far field. The circular geometry enables several other approaches to the diffraction calculation, such as using Babinet’s Principle to replace the definite integral in Equation 3 with one over the complementary finite domain.

The second important exception is that, in the spatial domain, coherence of incoming rays around the occulter leads to constructive interference and a non-intuitive “Arago spot” (Arago 1819) along the centerline of the instrument. Famously, the spot from a point source and circular disk in ideal geometry forms a J_0 Bessel function with peak value equal to the intensity of the incident light (e.g., Born & Wolf 1999; Reisinger et al. 2017).

For small beam deviations from the centerline, the Arago spot remains nearly unchanged, and a simple occulting disk therefore forms a real image of a distributed incident light source, convolved with a Bessel function spot profile on-axis and a compact elliptical evolute form off-axis (Coulson & Becknell 1922; Harvey & Forgham 1984). This is the basis of the field of Fresnel zone-plate imaging (e.g., Hecht & Zajac 1974; Davila 2011). Single-disk occulters therefore also act as pinhole cameras, forming a real image of the Sun at the center of the occulted shadow. But zone-plate imaging isn’t relevant to circular multi-edge occulters. The solar image is destroyed by the multiple scattering events, at least in the SPW approximation used to derive Equation 29. Each disk in the occulter scatters slightly converging rays from the prior disk, eliminating whatever image information may in principle be present after the first scattering event. The central bright spot from a multi-disk occulter is therefore just that – a single spot with an approximate Bessel function profile.

The Arago spot size may be estimated directly using a variation of Fraunhofer interference. In Section 3, we discussed the formation of directional fringes in the Fresnel-diffracted light around an edge. In the case of the Arago spot, light from opposite sides of the circular occulter interferes constructively at the central axis as in Figure 9. Under small offsets, the two beams go out of phase. Opposite sides of the “bright ring” illuminating the point of interest go fully out of phase when $h\phi = \lambda/4$. The ring as a whole exhibits full cancellation when $h\phi = \lambda/2\sqrt{2}$, with the additional $\sqrt{2}$ arising from the amount of total edge length at each vertical offset around the perimeter of the occulter. So the Arago spot behind a multi-disk occulter has a size given by:

$$r_A = \phi_0 (D - L) \approx \frac{\lambda (D - L)}{2\sqrt{2}h_n}, \quad (52)$$

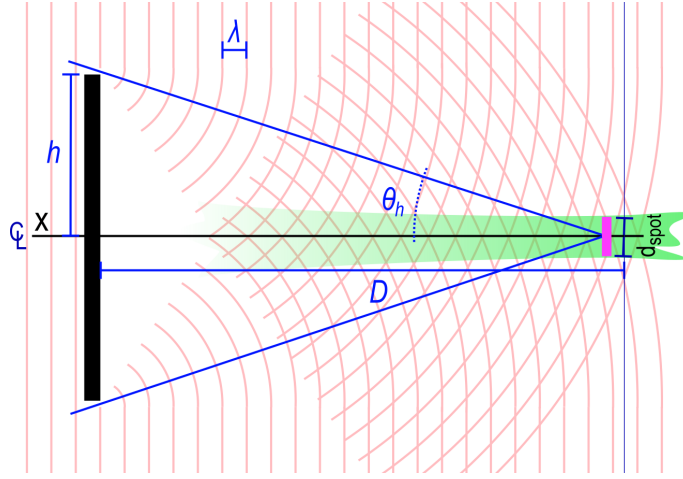


Figure 9. The Arago spot is a counterintuitive optical phenomenon that arises from interference around the periphery of a circular occulter. The occulter from Figure 1 is revolved about the X axis. Huygens' wavelets from around the entire edge of the occulter interfere constructively at a small locus along the centerline of the shadow. The width of this bright spot is determined by Fraunhofer-style interference between the contributions from opposite sides of the occulter.

where r_A is the radius of the spot, ϕ_0 is the radius of the edge of the spot, $D - L$ is the distance from the final disk to the location where the spot is measured, and h_n is the radius of of the final disk in the multi-disk occulter.

As an example, an instrument operating at $\lambda = 650$ nm, with $D - L = 175$ mm, and $h = 10$ mm would have an Arago spot diameter of $4 \mu\text{m}$ at the aperture. A single-disk device operating on a 10 mm aperture would thus have a minimum attenuation coefficient of order 10^{-7} from its Arago spot alone. Occulters with n disks, operating in the SPW regime, generate Arago spots with intensity that is attenuated by the effect of the first $n - 1$ disks, and the residual Arago spot is therefore usually negligible in its overall contribution.

Far from the Arago spot, interference effects may be neglected and incident diffracted beams on different parts of the aperture may be treated as incoherent. Considering a single 2-D cross-section of a circular aperture (as pictured in Figure 6), one may consider I_{obs} at the aperture to be a function of y . Varying y only affects the final attenuation from bending around the final (n^{th}) disk and not the geometry nor attenuation from disks 1 through $n - 1$; thus,

$$I_{obs}(y) = I_0 \mathcal{A}_f \mathcal{M} \left(\left[\Delta\Theta + \frac{R - y}{D - L} \right] \sqrt{\frac{\pi(D - L)}{\lambda}} \right), \quad (53)$$

where \mathcal{A}_f is the overall attenuation from the first $n - 1$ disks of the occulter. Migrating from 2-D to 3-D by revolving around the x axis, the average scattered intensity across the aperture is the integral of contributions from each y value, divided by the total area of the aperture. Thus,

$$I_{ap} = \frac{I_0 h \mathcal{A}_f}{R} \int_{-R}^R \mathcal{M} \left(\left[\Delta\Theta + \frac{R - r}{D - L} \right] \sqrt{\frac{\pi(D - L)}{\lambda}} \right) dr, \quad (54)$$

where the the variable of integration is r instead of y to reflect that the 2-D system of Equation 53 has been revolved around the x axis for a circular occulter and aperture. Two irregularities stand out: Equation 54 has an R in the denominator and lacks an expected πr in the integrand. The denominator R arises because the average covers twice the area of the aperture, i.e. $2\pi R^2$. This cancels with a factor of $2\pi R$ in the numerator to yield the R . The factor of $2\pi R$ and the lack of a $2\pi r$ under the integral both arise because light scattered into each portion of the aperture is treated as the incoherent sum of contributions of light from all around the aperture, and stray light is therefore concentrated near the center of the aperture. This yields a factor of R/r in the integrand, canceling out the expected r ; and the remaining $2\pi R$ is constant and migrates outside the integral. The concentration effect is similar to, but distinct from, the Arago spot itself: the Arago spot is formed by the *coherent* concentration of electric field from all around the periphery of the occulter; while this far less pronounced effect is due to the *incoherent* concentration of visible flux from all around the periphery, and merely equalizes the contribution of each radius across the full aperture.

Because \mathcal{M} varies rapidly with its angular argument over the long throw between the occulter and the aperture, the aperture-average scattered-light intensity in Equation 54 is dominated by the outermost (high- r) portion of the aperture. The sharpness of this bright outer boundary in the spatial domain is determined by the specific geometry of the instrument. Fortunately, Equation 54 is straightforward to evaluate numerically for any given geometry.

For initial occulter design, where precision is less important than rapid evaluation, one may neglect the integral in Equation 54 entirely, and consider all of the final disk's diffracted light to land on the outermost edge of the aperture. This simplification yields

$$I_{ap} \approx \frac{I_0 h A_f}{R} \mathcal{M} \left(\Delta \Theta \sqrt{\frac{\pi(D-L)}{\lambda}} \right), \quad (55)$$

which is really just

$$I_{ap} \approx I_{obs} \frac{h}{R} \quad (56)$$

where I_{obs} is taken from Equation 34. In other words, to a reasonable and somewhat conservative approximation, all of the scattered light around the occulter is focused onto a ring around the outside of the aperture (neglecting the Arago spot, which is very bright but also very small), and the average diffracted intensity across the aperture may be approximated by scaling the basic SPW calculation for a simple multi-vane barrier in 2-D.

Solar disk occulters in general are not obstructing a point source, but rather the Sun itself. Therefore, Equation 34 only applies if the apparent size of the Sun is small compared to the apparent size of the occulter as seen from the instrument focusing optics. This is the case for typical linear geometries (heliospheric imagers), but not for typical coronagraph geometries. Fortunately, the problem of a distributed source is exactly analogous to the problem of a distributed aperture, and the same design approximation may be used on the input side of the occulter as the output side. The same process may be followed for the disk of the Sun, as for the aperture. This yields an equation similar to Equation 54, but with the integral running over entrance angle rather than aperture location; and for design purposes it is a helpful and conservative assumption to treat the Sun as a bright ring. Treating both the Sun and aperture as rings rather than disks yields a complete design equation for multi-disk solar occulters in the SPW approximation:

$$I_{ap} = I_0 \frac{\Theta_{\odot} R}{\Theta_{in} h} \mathcal{M} \left([\Theta_{in} - \Theta_{\odot}] \sqrt{\pi \Delta L / \lambda} \right) \left[\mathcal{M} \left(\Delta \Theta \sqrt{\pi \Delta L / \lambda} \right) \right]^{n-2} \mathcal{M} \left(\Delta \Theta \sqrt{\pi(D-L)/\lambda} \right), \quad (57)$$

which echoes Equation 34 for the circular case. Here, I_{ap} is again the aperture-averaged intensity of diffracted light; Θ_{\odot} is the apparent solar radius; Θ_{in} is the design acceptance angle of the occulter, i.e. the largest angle from centerline that the occulter is designed to hide; R is the radius of the aperture; h is the radius of the final disk of the occulter; \mathcal{M} is defined in Equation 30; ΔL is the distance between disks on the occulter; n is the number of disks in the occulter; L is the overall length of the occulter; D is the distance from the front of the occulter to the aperture; and λ is the operating wavelength. Taking $\Delta \Theta \sqrt{\Delta L / \lambda} \ll 1$, and expanding $\mathcal{M}(\gamma)$ to first order, yields an even simpler design equation, in the sense that most of the transcendental calculations are eliminated.

$$I_{ap} = \frac{I_0 \Theta_{\odot} R}{4^{n-1} \Theta_{in} h} \left[1 - 8 (\Theta_{in} - \Theta_{\odot}) \sqrt{\Delta L / \pi \lambda} \right] \left[1 - 8 \left(\Delta \Theta \sqrt{\Delta L / \pi \lambda} \right) \right]^{n-2} \mathcal{M} \left(\Delta \Theta \sqrt{\pi(D-L)/\lambda} \right) \quad (58)$$

Equation 58 is a closed-form expression but still contains the transcendental $\mathcal{C}(\gamma)$ and $\mathcal{S}(\gamma)$ functions, embedded in the $\mathcal{M}(\gamma)$ function that forms the final coefficient. It is of course possible to approximate even further and eliminate the transcendentals to simplify the design process. Ignoring the advantage of the longer ($D-L$) throw at the exit of the occulter yields a conservative estimate with no transcendental functions at all:

$$I_{ap} \approx \frac{I_0 \Theta_{\odot} R}{4^n \Theta_{in} h} \left[1 - 8 (\Theta_{in} - \Theta_{\odot}) \sqrt{\Delta L / \pi \lambda} \right] \left[1 - 8 \left(\Delta \Theta \sqrt{\Delta L / \pi \lambda} \right) \right]^{n-1}. \quad (59)$$

Equation 59 is a complete closed-form solution estimating the overall attenuation of an n -disk externally occulted solar coronagraph with prescribed geometry, subject to the limits of the SPW approximation as described in Section 4.2. In the condition where $\Delta \Theta \sqrt{\Delta L / \pi \lambda} < 1$, Equation 59 is always conservative compared to the full SPW treatment embodied in Equation 57, and may therefore be used for initial design estimation.

6. DISCUSSION AND CONCLUSIONS

We have developed a simplified theory of occulter performance, suitable for understanding the behavior of multi-vane linear or corral-baffle occulters (for heliospheric imagers), or multi-disk circular occulters (for externally occulted coronagraphs), in a design regime that is typical for existing and planned instrumentation. The successive plane wave (SPW) approximation represents a “middle ground” solution for calculating the diffraction scattering around multiple-edge occulters. Based on the SPW approach, we have identified the ideal envelope for a multi-edge occulter: a circular-cross section cylinder or ogive, in linear or circular geometry respectively. We have also explained the quasi-achromatic fringes that are observed around multi-edge external occulters in modern instrumentation. By exploring the limits of the SPW approach, we have identified a fundamental limit to occulter performance within a prescribed instrument size and angular offset, explaining why high- n solutions and smooth occulters do not perform as well as the naïve first-order theory or SPW approximation predict. Further, we have developed a formula indicating the highest number of edges that are useful for a given occulter geometry, before the point of diminishing returns is reached. We have also touched on the reasons for the surprisingly good performance of conical-profile multi-disk coronagraph occulters: even in the simple SPW approximation to the total wave theory, the intermediate disks interact with the extended wave field of diffracted light near the occulter, despite not protruding into the ray-approximation beam passing around each disk.

In circular geometry, we have explored the brightness and overall flux of the Arago spot formed by coherent interference around an occulter, affirmed the known result that the Arago spot is important for single-disk designs, and identified why the spot is negligible for multi-disk designs. In particular, in multi-disk designs the Arago spot is attenuated by the action of the $n - 1$ disks preceding the last one, and is therefore reduced by a large factor in brightness compared to a single-disk system. We have also discussed the incoherent concentration of diffracted light by the circular geometry of the occulter, even outside the Arago spot. We have identified analytically the brightness pattern expected across the aperture of a multi-disk externally occulted coronagraph. Finally, we have generated conservative design estimation formulae that permit iterative design of novel instruments via closed-form analytic expressions to estimate occulter performance, along with slightly more complex formulae that may be applied to model the stray light from a chosen design. The conservatism of the estimation formulae is important, because of the known sensitivity of multi-disk occulter performance to small misalignments. These formulae do not require explicit simulation of the electromagnetic field (or, equivalently, numeric integration of the Kirchoff integral), yet still capture enough of the physics of occulter behavior to both advance intuition and yield predictive power for new designs.

Occulter design is only one element of either heliospheric imager or coronagraph design. Even fully externally occulted designs require considering scattering in the remainder of the instrument including the focusing optics and detector system, which scatter the “bright line” or “bright ring” from the external occulter into broader stray light patterns at the focal plane. Further, both types of instrument view a faint object – the Sun’s K corona – against a much brighter background comprising a mix of sky brightness, the solar F corona, and the starfield in addition to any instrumental stray light. Coronagraph images must thus be post-processed to remove all of these sources of brightness, in order to reveal the K corona; precise photometry and careful post-processing are therefore required regardless of the level of instrumental stray light.

Even a highly simplified wave theory such as the successive plane wave treatment has predictive and explanatory power for the behavior of multi-disk occulters. By exploring the limits of this approximation, we have been able to explain and quantify several aspects of occulter behavior – achromatic fringing, the limits of multi-disk performance, and the *lack* of degradation, in circular geometry, from the Arago spot in multi-disk coronagraphs. Further, the successive-plane-wave treatment has sufficiently well defined limits of applicability, that it may be used to inform future instrument designs in both linear and circular geometry.

This work was partially funded by the NASA/NOAA Space Weather Next program, Contract No. 80GSFC23CA056x, and partially funded internally by Southwest Research Institute under its Internal Research & Development program. The authors gratefully acknowledge helpful comments from several members of the coronagraph instrument community, including C. Aime, R. Howard, and A. Thernisien.

REFERENCES

- Aime, C. 2007, *A&A*, 467, 317,
doi: [10.1051/0004-6361:20066789](https://doi.org/10.1051/0004-6361:20066789)
- . 2020, *A&A*, 637, A16,
doi: [10.1051/0004-6361/201937208](https://doi.org/10.1051/0004-6361/201937208)

- Arago, F. 1819, *Annales de Chimie et de Physique*, 11, 5
- Baccani, C., Landini, F., Romoli, M., et al. 2016, in *Society of Photo-Optical Instrumentation Engineers (SPIE) Conference Series*, Vol. 9904, *Space Telescopes and Instrumentation 2016: Optical, Infrared, and Millimeter Wave*, ed. H. A. MacEwen, G. G. Fazio, M. Lystrup, N. Batalha, N. Siegler, & E. C. Tong, 990450, doi: [10.1117/12.2232534](https://doi.org/10.1117/12.2232534)
- Billings, D. E. 1966, *A guide to the solar corona*
- Born, M., & Wolf, E. 1999, *Principles of Optics*, 7th Ed. (Cambridge University Press), 31–33
- Bout, M., Lamy, P., Maucherat, A., Colin, C., & Llebaria, A. 2000, *ApOpt*, 39, 3955, doi: [10.1364/AO.39.003955](https://doi.org/10.1364/AO.39.003955)
- Breault, R. P. 1977, in *Society of Photo-Optical Instrumentation Engineers (SPIE) Conference Series*, Vol. 107, *Stray-light problems in optical systems*, ed. J. D. Lytle & H. Morrow, 2, doi: [10.1117/12.964591](https://doi.org/10.1117/12.964591)
- Brueckner, G. E., Howard, R. A., Koomen, M. J., et al. 1995, *SoPh*, 162, 357, doi: [10.1007/BF00733434](https://doi.org/10.1007/BF00733434)
- Buffington, A. 2000, *Applied Optics*, 39, 2683
- Buffington, A., Hick, P. P., Jackson, B. V., & Korendyke, C. M. 1998, in *Missions to the Sun II*, ed. C. M. Korendyke, Vol. 3442, *International Society for Optics and Photonics (SPIE)*, 77 – 86, doi: [10.1117/12.330266](https://doi.org/10.1117/12.330266)
- Coulson, J., & Becknell, G. G. 1922, *Physical Review*, 20, 594, doi: [10.1103/PhysRev.20.594](https://doi.org/10.1103/PhysRev.20.594)
- Davila, J. M. 2011, in *Solar Physics and Space Weather Instrumentation IV*, ed. S. Fineschi & J. Fennelly, Vol. 8148, *International Society for Optics and Photonics (SPIE)*, 81480O, doi: [10.1117/12.898956](https://doi.org/10.1117/12.898956)
- de Wijn, A. G., Burkepile, J. T., Tomczyk, S., et al. 2012, in *Society of Photo-Optical Instrumentation Engineers (SPIE) Conference Series*, Vol. 8444, *Ground-based and Airborne Telescopes IV*, ed. L. M. Stepp, R. Gilmozzi, & H. J. Hall, 84443N, doi: [10.1117/12.926511](https://doi.org/10.1117/12.926511)
- DeForest, C., Killough, R., Gibson, S., et al. 2022, in *2022 IEEE Aerospace Conference*, 1–11, doi: [10.1109/AERO53065.2022.9843340](https://doi.org/10.1109/AERO53065.2022.9843340)
- DeForest, C., Seaton, D. B., Caspi, A., et al. 2024, *Solar Physics*, 299, 78
- DeForest, C. E., Matthaeus, W. H., Viall, N. M., & Cranmer, S. R. 2016, *ApJ*, 828, 66, doi: [10.3847/0004-637X/828/2/66](https://doi.org/10.3847/0004-637X/828/2/66)
- Dudley, R., Krimchansky, A., Tadikonda, S., et al. 2023, in *EGU General Assembly Conference Posters* [also available via NASA's NTRS server], EGU–1714, doi: [10.5194/egusphere-egu23-1714](https://doi.org/10.5194/egusphere-egu23-1714)
- Erickson, N., Beasley, M., Smith, T. J., et al. 2025, *Astrophys. J.*, (In work)
- Evans, J. W. 1948, *Journal of the Optical Society of America* (1917-1983), 38, 1083
- Feynman, R. P., Leighton, R. B., & Sands, M. 1963, *The Feynman Lectures on Physics*, Vol. I (California Institute of Technology), 35–1—35–10
- Fort, B., Morel, C., & Spaak, G. 1978, *A&A*, 63, 243
- Gong, Q., & Socker, D. 2004, in *Optical Systems Degradation, Contamination, and Stray Light: Effects, Measurements, and Control*, Vol. 5526, *SPIE*, 208–219
- Harvey, J. E., & Forgham, J. L. 1984, *American Journal of Physics*, 52, 243, doi: [10.1119/1.13681](https://doi.org/10.1119/1.13681)
- Hecht, E., & Zajac, A. 1974, *Optics* (Addison-Wesley)
- Howard, R. A., Moses, J. D., Vourlidas, A., et al. 2008, *SSRv*, 136, 67, doi: [10.1007/s11214-008-9341-4](https://doi.org/10.1007/s11214-008-9341-4)
- Howard, R. A., Vourlidas, A., Colaninno, R., et al. 2020, *Astronomy & Astrophysics*, 642, A13
- Jackson, B. V. 1985, *SoPh*, 100, 563, doi: [10.1007/BF00158445](https://doi.org/10.1007/BF00158445)
- Koomen, M. J., Detwiler, C. R., Brueckner, G. E., Cooper, H. W., & Tousey, R. 1975, *Applied Optics*, 14, 743, doi: [10.1364/AO.14.000743](https://doi.org/10.1364/AO.14.000743)
- Landini, F., Vivès, S., Romoli, M., et al. 2012, in *Society of Photo-Optical Instrumentation Engineers (SPIE) Conference Series*, Vol. 8442, *Space Telescopes and Instrumentation 2012: Optical, Infrared, and Millimeter Wave*, ed. M. C. Clampin, G. G. Fazio, H. A. MacEwen, & J. Oschmann, Jacobus M., 844227, doi: [10.1117/12.926225](https://doi.org/10.1117/12.926225)
- Landini, F., Baccani, C., Schweitzer, H., et al. 2017, *Optics Letters*, 42, 4800, doi: [10.1364/OL.42.004800](https://doi.org/10.1364/OL.42.004800)
- Laurent, G., DeForest, C., Beasley, M., et al. 2025, *Sol. Phys.*, (In work)
- Lenskii, A. V. 1981, *Soviet Ast.*, 25, 366
- LightTrans. 2024, *VirtualLab Fusion software*, 2024.1. <https://lighttrans.com>
- Llebaria, A., Lamy, P., & Danjard, J. F. 2006, *Icarus*, 182, 281, doi: [10.1016/j.icarus.2005.12.013](https://doi.org/10.1016/j.icarus.2005.12.013)
- Lyot, B. 1930, *Bulletin Astronomique*, 6, 305
- Newkirk, G., & Bohlin, D. 1963, *Applied Optics*, 2, 131
- Photon Engineering. 2021, *FRED software*, 20.01. <https://photonengr.com/fred-software>
- Reisinger, T., Leufke, P. M., Gleiter, H., & Hahn, H. 2017, *New Journal of Physics*, 19, 033022, doi: [10.1088/1367-2630/aa5e7f](https://doi.org/10.1088/1367-2630/aa5e7f)

- Rougeot, R., Aime, C., Baccani, C., et al. 2018, in Society of Photo-Optical Instrumentation Engineers (SPIE) Conference Series, Vol. 10698, Space Telescopes and Instrumentation 2018: Optical, Infrared, and Millimeter Wave, ed. M. Lystrup, H. A. MacEwen, G. G. Fazio, N. Batalha, N. Siegler, & E. C. Tong, 106982T, doi: [10.1117/12.2313258](https://doi.org/10.1117/12.2313258)
- Shirley, E. L., & Datla, R. 1996, Journal of research of the National Institute of Standards and Technology, 101, 745
- Thernisien, A., Colaninno, R. C., Plunkett, S., et al. 2005, in Society of Photo-Optical Instrumentation Engineers (SPIE) Conference Series, Vol. 5901, Solar Physics and Space Weather Instrumentation, ed. S. Fineschi & R. A. Viereck, 366–376, doi: [10.1117/12.614567](https://doi.org/10.1117/12.614567)
- Thernisien, A., Carter, M., Chua, D., et al. 2021, in AGU Fall Meeting Abstracts, Vol. 2021, SH43B–08
- Thernisien, A. F. R., Howard, R. A., Korendyke, C., et al. 2018, in Society of Photo-Optical Instrumentation Engineers (SPIE) Conference Series, Vol. 10698, Space Telescopes and Instrumentation 2018: Optical, Infrared, and Millimeter Wave, ed. M. Lystrup, H. A. MacEwen, G. G. Fazio, N. Batalha, N. Siegler, & E. C. Tong, 106980E, doi: [10.1117/12.2313645](https://doi.org/10.1117/12.2313645)
- Vourlidas, A., Howard, R. A., Plunkett, S. P., et al. 2016, Space Science Reviews, 204, 83
- Wang, W., Zhang, X., Meng, Q., & Wang, D. 2021, Optics Express, 29, 2953, doi: [10.1364/OE.408524](https://doi.org/10.1364/OE.408524)
- Yang, H., Bong, S.-C., Cho, K.-S., et al. 2018, Journal of Korean Astronomical Society, 51, 27, doi: [10.5303/JKAS.2018.51.2.27](https://doi.org/10.5303/JKAS.2018.51.2.27)